

IR-photon quenching of delayed electron detachment from hot pentacene anionsS. Iida ¹, S. Kuma ², M. Kuriyama ¹, T. Furukawa ³, M. Kusunoki,³ H. Tanuma ¹, K. Hansen ⁴,
H. Shiromaru,⁵ and T. Azuma ^{2,1,*}¹*Department of Physics, Tokyo Metropolitan University, Hachioji, Tokyo 192-0397, Japan*²*Atomic, Molecular and Optical Physics Laboratory, RIKEN, Wako, Saitama 351-0198, Japan*³*Department of Physics, Toho University, Funabashi, Chiba 274-8510, Japan*⁴*Center for Joint Quantum Studies and Department of Physics, School of Science, Tianjin University, Tianjin 300072, China*⁵*Department of Chemistry, Tokyo Metropolitan University, Hachioji, Tokyo 192-0397, Japan*

(Received 12 July 2021; revised 29 September 2021; accepted 30 September 2021; published 27 October 2021)

Spontaneous and photoinduced delayed electron detachment from pentacene anions was measured in the electrostatic ion storage ring TMU E-ring. The dissipation mechanisms of the internal energy of the stored hot ions were inferred both from the temporal profile of the spontaneous detachment and from the laser-firing time dependence of the photoinduced temporal profile. Simulations based on statistical emission processes reproduced the observed behaviors, providing the value for the radiative cooling rates in the time range of a few tens of milliseconds. Using the obtained information on the competition between electron detachment and radiative cooling, we discuss the anion survival probabilities as a function of the initial internal energies and the nature of the observed quasiexponential decrease in the temporal profile of the spontaneous detachment at long times.

DOI: [10.1103/PhysRevA.104.043114](https://doi.org/10.1103/PhysRevA.104.043114)**I. INTRODUCTION**

Isolated molecular ions excited by photon absorption may undergo fluorescence or prompt thermalization (often on the picosecond time scale), i.e., statistical redistribution of the total internal energy into vibrational modes through internal conversion (IC). After thermalization the excitation energy is dissipated via three possible channels: evaporation of small fragments, thermionic electron emission, or radiation emission. These mechanisms for energy dissipation of hot molecular ions in the gas phase have been intensively investigated for more than a decade using ion storage rings and ion traps [1–4]. For example, a series of studies focusing on the family of negative linear carbon clusters revealed that infrared (IR) radiative cooling via the IC process is dominant for C_5^- , C_6H^- , and C_7^- molecules [5–7], whereas electronic radiative cooling with visible-photon or near-IR-photon emission, often called recurrent fluorescence (RF), is the dominant photon emission channel for C_4^- and C_6^- [7–10]. RF is emitted from the thermally populated electronically excited state via the inverse internal conversion (IIC). Relative to emission of IR photons, the much larger dipole oscillator strength of visible-photon or near-IR-photon emission compensates for the suppression of these channels caused by their smaller statistical weight.

These previous studies have examined small, carbon-containing molecular anions, in which electron detachment often dominates over fragmentation. This makes the interpretation of the emission processes more straightforward than it is for decays of cations, where different, potentially competing fragmentation channels have to be considered. In this paper,

we investigate the larger pentacene molecular anion ($C_{22}H_{14}^-$), a member of the polycyclic aromatic hydrocarbon (PAH) family with mass 278 u. The spectroscopy and photophysics of PAHs in the gas phase are active research fields in astrophysics and astrochemistry [11,12]. RF has been found to be an important cooling mechanism for several PAH cations [13–18], similar to the previous identification of radiative cooling as an important stabilizing factor suppressing fullerene decay [19,20]. In contrast, little experimental information on these delayed processes for PAH anions has been obtained so far [21]. One of the possible reasons for this shortage of information is that gas-phase PAH anions are not readily prepared in the laboratory. On the other hand, it has been proposed that the majority of the negative charge carriers in interstellar molecular clouds are in the form of PAH anions [22,23]. The pentacene anion is of special interest in this context because it has an electronic excited state, which exhibits exceptionally strong absorption, slightly below the electron detachment threshold E_{th} [24].

Here, we report measurements of the spontaneous and laser-induced delayed electron detachment from hot pentacene anions stored in the electrostatic ion storage ring TMU E-ring. The signatures associated with radiative cooling processes are discussed with the aid of model simulations based on a statistical description of the decays.

II. PROPERTIES OF THE PENTACENE ANION AND NEUTRAL

The ground state of the pentacene anion belongs to the D_{2h} symmetry point group and has the electronic configuration $\dots \pi(b_{2g})^2 \pi(b_{1u})^1$, corresponding to a ${}^2B_{1u}$ doublet ground state. The axis definition for the structure of

*toshiyuki-azuma@riken.jp

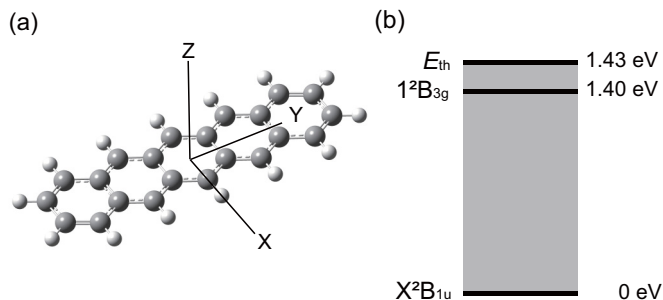


FIG. 1. (a) Structural representation of the pentacene anion placed in the XY plane. Carbon and hydrogen atoms are shown in gray and white, respectively. (b) Energy level diagram of the pentacene anion showing the electron detachment threshold E_{th} and the electronic excited state below E_{th} .

the molecule, which is used for the irreducible representations of the vibrational modes listed in Tables I and II in the Appendix, is shown in Fig. 1(a).

The value of E_{th} has been determined to be 1.43 eV by laser-induced detachment experiments [25]. The absorption peak of the pentacene anion in a cold matrix was reported to be centered at 885 nm (1.40 eV) in 2-methyltetrahydrofuran (MTHF) [24], and in inert gas matrices the absorption peak was centered at 872.6 nm for Ne, 882.1 nm for Ar, and 886.4 nm for Kr [26]. Gas-phase absorption data are so far not available. In the present experiment we observed an enhancement in the neutral yield at around 890 nm (= 1.39 eV) during a wavelength scan using an optical parametric oscillator (OPO) laser, motivating the use of this wavelength for the excitation. The neutrals produced in the ring are most likely produced by electron detachment of pentacene anions. That is, electron detachment is expected to be dominant over fragmentation because E_{th} is much lower than the dissociation threshold (the smallest bond dissociation energy is about 4 eV [27]). In fact, an electron attachment mass spectroscopic study has shown that dissociation does not occur below a collision energy of 5 eV, corresponding to about 6 eV (5 eV + electron affinity) internal energy of the produced pentacene anion [21]. Hirata *et al.* calculated the oscillator strength of the transition $1^2B_{3g} \leftarrow X^2B_{1u}$ to be 0.241 [28]. In the present simulation, we employed this value of 0.241 along with the level energies of 1.40 and 1.43 eV for 1^2B_{3g} and E_{th} , respectively, as shown in Fig. 1(b). Other excited states were also calculated [28]; however, we did not take them into account, because their oscillator strengths are negligibly small.

The ground-state geometries of both the pentacene neutral and the pentacene anion were optimized with density functional theory, applying the nonlocal hybrid Becke three-parameter Lee-Yang-Parr functional (B3LYP) [29,30] and the 6-311+G(2d,2p) basis set. These calculations were performed using the quantum chemistry software package GAUSSIAN09 [31]. They also provided the IR frequencies and intensities of the vibrational modes. From these values, Einstein A coefficients for each transition were calculated. In Table I in the Appendix, the IR frequencies of the 102 vibrational modes of the neutral molecule are listed, and those of the anion are given in Table II together with the Einstein A coefficients. The modes with optically forbidden transitions were needed

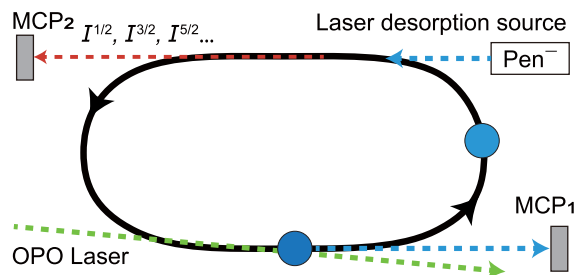


FIG. 2. Schematic of the experimental setup. Stored pentacene anions were photoexcited by the OPO laser, which intersected the anion beam at a small angle to avoid hitting MCP₁ (dumped-ion-beam detector). The neutral species generated in the upper straight section were detected with MCP₂.

for the evaluation of the density of states in the statistical approach simulation. The frequencies obtained in the present work were compared with previous theoretical [32] and experimental works (matrix isolation infrared spectra in an argon matrix) [33,34], and the discrepancy was found to be within a few percent on average.

III. EXPERIMENTS

A schematic of the experimental setup is shown in Fig. 2. The details are given in Ref. [35], and only the specifics for the present experiment are given here. Pentacene anions were produced with a laser desorption source. The ablation target was pentacene powder pressed into a flat pellet. It was irradiated by a 532-nm pulsed Nd:YAG laser of 10-Hz repetition rate. The laser energy was reduced to 0.4 mJ/pulse, which is substantially below the fluence used to produce linear carbon cluster anions C_n^- by ablation of graphite in the same source [5–7,9,10]. The ions produced were accelerated to 15 keV kinetic energy and injected into the electrostatic ion storage ring TMU E-ring, where they circulated with a period of 76.4 μ s. The pentacene anions were mass selected during storage by removing unwanted coaccelerated ions with the application of a kick pulse on one of the deflection electrodes at 707.8 μ s after injection. As mentioned in the previous section, the excitation spectrum of the stored anions was consistent with the known absorption spectra of pentacene anions [24,26], verifying that the stored anions were not isobars (for example, a H-loss fragment with one ^{13}C). The non-negligible width of the velocity distribution will cause the ion bunch to gradually spread with storage time, which is undesirable for the pulsed-laser merging experiment. To prevent this debunching, an rf voltage synchronized with the passage of the ions was applied to a cylindrical buncher electrode to maintain an ion bunch of width 2 μ s, as described in Ref. [35].

After a preset storage time, the ions were photoexcited with a wavelength-tunable nanosecond OPO laser (890 nm, about 1 mJ/pulse with a repetition rate of 10 Hz, i.e., one laser pulse per ion injection) along one of the straight sections of the ring. The neutral particles produced by laser-induced electron detachment were detected using a microchannel plate (MCP) detector placed at the extension of the straight section of the ring opposite to the laser merging side. Thereby, the

observed neutral particles are the delayed component after laser irradiation. We confirmed that delayed events are due to the absorption of single photons under the present laser intensity by checking the linear dependence of enhancement in neutral signals against the laser fluence. The yields for each turn after the laser pulse are integrated and denoted $I^{1/2}$, $I^{3/2}$, $I^{5/2}$, ..., with the superscript signifying the time of detection after the photon absorption in units of the circulation period. In addition to the laser-induced detachment, we also observed spontaneous detachment right after ion injection into the ring, and at every subsequent passage of the ions through the detector side.

It should be noted that neutrals produced upon photoexcitation are detected only when electron detachment occurs in the straight section of the ring along which the detector is placed. This means that the detected signal is proportional to the decrease in the number of the surviving ions during the time they spend in this straight section, i.e.,

$$I \propto N(t_1) - N(t_2), \quad (1)$$

where t_1 and t_2 are the times of entry into and departure from the straight detection section, respectively, and $N(t)$ is the number of stored ions at time t . The constant of proportionality is the time- and energy-independent transmission and detection probability. From the revolution time of the 15-keV pentacene anion beam in the ring (76.4 μ s) and the length of the straight section of the ring (1.95 m), the time window for detection of the $I^{1/2}$ event after a half circulation is calculated to be 28.6–47.8 μ s. In general, the time windows for the $(1/2 + n)$ th passage of the detection section are then $(28.6 + 76.4n)$ μ s to $(47.8 + 76.4n)$ μ s. As shown later, the time window is converted to an energy window, i.e., the energy range to be surveyed, based on the energy-dependent detachment rates.

In order to estimate the background counts of neutrals attributed to collision-induced electron detachment, the time-dependent number of stored ions is needed. The standard procedures of using either the neutral yield resulting from collisions of the stored ions with residual gas or the pickup signal induced by ion passage through the pickup electrode are not applicable in the present study. The spontaneous detachment component overwhelms the collision-induced neutral yield at times earlier than 40 ms, and the pickup signal suffers from the small number of stored ions (less than 1000 per bunch at injection). The number of stored ions was instead counted by the beam-dump technique, i.e., extraction of stored ions from the ring, by switching off the voltage of the relevant 10° deflector at a series of times 10–80 ms after ion injection. The detection efficiency of the MCP was greatly reduced by lowering the applied voltage, keeping the count rate to less than 0.1 per ion dumping cycle to avoid saturation of the ion counts. Note that this is the case exclusively for the beam dump.

IV. SIMULATION PROCEDURE

Two complementary simulations were conducted. The first, a simulation of the time-dependent energy distribution of the anion ensemble, was based on the energy-dependent cooling power. The purpose was to obtain the radiative cooling

rates of pentacene anions from the observed electron detachment (neutralization) yields, both spontaneous and photon induced. This simulation did not track the history of individual molecules. The initial energy distribution was parametrized by an initial effective temperature $T_{\text{eff}}^{\text{ini}}$, which was used to generate a distribution akin to a canonical distribution. This procedure has previously been successfully applied to the description of similar experiments on small anions such as C_4^- , C_6^- , and C_6H^- [7,9,10,36].

In the other simulation, using the obtained cooling rates, the fate of the anions experiencing competition between electron detachment and radiative cooling was traced with a Monte Carlo simulation. That is, we evaluated the survival probability $f(E_{\text{ini}})$ of ions with initial internal energy E_{ini} by generating random numbers corresponding to one of several possible events, i.e., electron detachment or radiative cooling via photons of a certain energy. Such events were successively generated, with no regard for elapsed time, until either electron detachment took place or the internal energy decreased below E_{th} . Note that the two approaches employed the same values for inputs, and they complementarily show different aspects of the same dynamics. In this section, the details of these simulation procedures are explained. Note that the vibrational radiative decay rate constants contain a correction factor to be determined later, while the optimized value is adopted in advance of the demonstrated results.

A. Rate constants and cooling power

The electron detachment rate constant k_d for different internal energies E was calculated based on the principle of detailed balance theory [37] as follows:

$$k_d(E) = \int_0^{E-E_{\text{th}}} \frac{2m}{\pi^2 \hbar^3} \sigma_c(\epsilon) \epsilon \frac{\rho_d(E - E_{\text{th}} - \epsilon)}{\rho_p(E)} d\epsilon, \quad (2)$$

where m and ϵ are the mass and kinetic energy of the electron, respectively. $\sigma_c(\epsilon)$ is the kinetic-energy-dependent capture cross section, which was evaluated using the Langevin cross section $\pi e \left(\sqrt{\frac{2\alpha}{4\pi\epsilon_0\epsilon}} \right)$. The polarizability volume α was calculated to be 50.4 \AA^3 for the optimized geometry of the neutral molecule using GAUSSIAN09 software [31]. ρ_d and ρ_p are the densities of states of the daughter (neutral) and parent (anionic) pentacene, respectively, and were calculated assuming that all vibrations are harmonic. The electronic degeneracies of the parent and daughter were included in their densities of states, and the spin degeneracy for the emitted electron is given by the numerical factor of 2 in Eq. (2). The calculated detachment rate constant $k_d(E)$ as a function of the internal energy E is shown in Fig. 3(a).

From the time windows for detection of $I^{1/2}$, we derived the corresponding detachment rate constant of $2.6 \times 10^4 \text{ s}^{-1}$. Using the relation of k_d with the internal energy shown in Fig. 3(a), the energy window $E_0^{1/2}$ is calculated to be 3.5 eV with a FWHM of 0.55 eV. The relatively large width of the energy window compared with, for example, the smaller molecules C_4^- and C_6^- is due to the larger heat capacity of pentacene, which results in a slower variation of k_d with energy [7,9,10]. Both the value of the centroid and the FWHM decrease for subsequent turns in the ring.

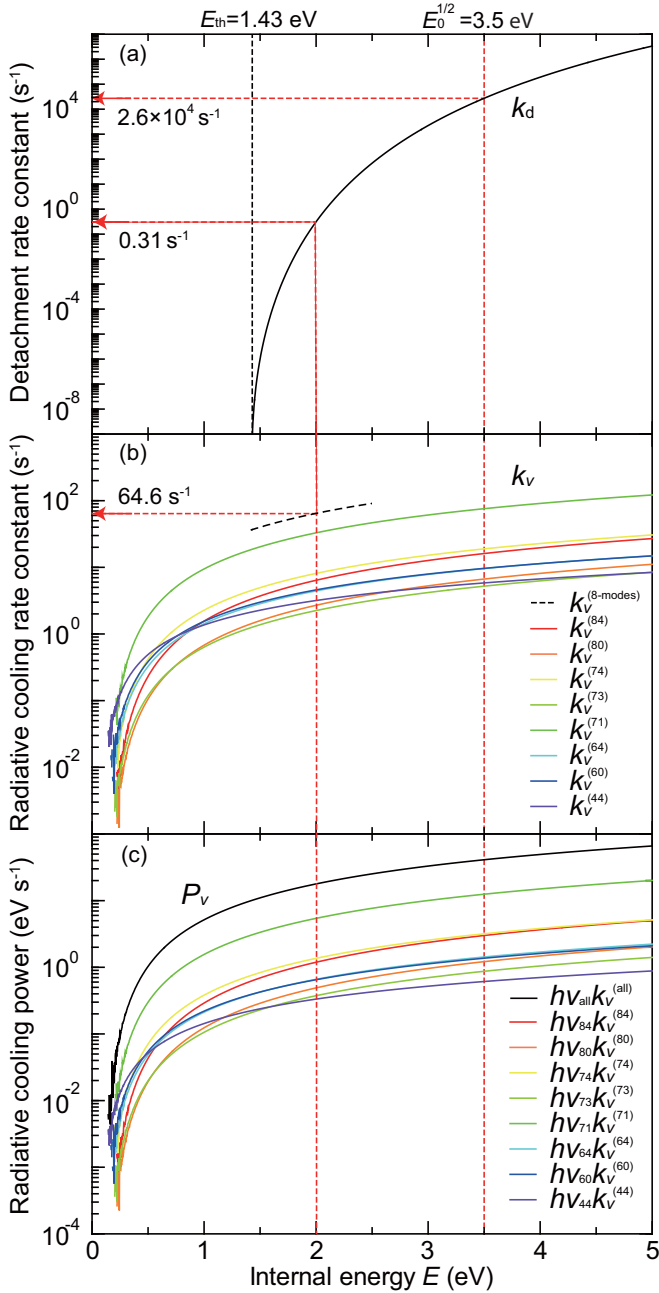


FIG. 3. (a) Detachment rate constant k_d (s^{-1}) as a function of internal energy E . E_{th} represents the electron detachment threshold of 1.43 eV. $E_0^{1/2}$ of 3.5 eV refers to the center of the energy window with FWHM of 0.55 eV for neutral detected after one half revolution. (b) Calculated vibrational radiative cooling rates $k_v^{(i)}$ as a function of internal energy E , for eight major vibrational modes in the rate constants $i = 84$ (1503.4 cm^{-1}), 80 (1470.3 cm^{-1}), 74 (1355.6 cm^{-1}), 73 (1347.1 cm^{-1}), 71 (1328.6 cm^{-1}), 64 (1202.6 cm^{-1}), 60 (1145.4 cm^{-1}), and 44 (845.9 cm^{-1}). The k_d and the sum of the rate constants of these modes $k_v^{(8\text{-modes})}$ at around 2 eV, shown by the dashed black line, are discussed in Sec. VB. The structures of $k_v^{(i)}$ at internal energies E less than 0.3 eV are attributed to the finite small internal energy to be distributed to each vibrational mode. (c) Calculated total vibrational cooling power, P_v (black), and the eight main contributions, $h\nu_i k_v^{(i)}$ (other colors), as a function of internal energy E .

The photon emission rate constant $k_v^{(i)}(E)$ of the vibrational transition for the i th vibrational mode is given by

$$k_v^{(i)}(E) = S_v A_{1-0}^{(i)} \frac{1}{\rho(E)} \sum_n \rho(E - nh\nu_i). \quad (3)$$

Here, n is the vibrational quantum number, ν_i is the vibrational frequency of the i th mode, and ρ is the density of states taking account of all the vibrational modes. It is noted that this expression is simplified but mathematically identical to the previous one in Refs. [1,9,33,34]. $A_{1-0}^{(i)}$ are the Einstein A coefficients for the vibrational transitions, and S_v is a correction factor to be determined as a fitting parameter. Among the 102 vibrational modes of the pentacene anion, only a few play an important role in radiative cooling, as will be shown later. The contribution from electronic cooling (recurrent fluorescence) is negligible because the state density of the electronic excited state is a factor of about 10^{-9} lower than that of the electronic ground state at $E_0^{1/2}$. This is reasonable considering the absence of any low-lying electronically excited state. In Fig. 3(b), we show the internal energy dependence of vibrational cooling rates of the eight main contributing modes.

The vibrational energy emission rate P_v is then

$$P_v(E) = \sum_i h\nu_i k_v^{(i)}(E). \quad (4)$$

The energy-dependent vibrational radiative cooling power $P_v(E)$ from all modes, calculated using Eq. (4), is plotted in Fig. 3(c), together with the individual contributions $h\nu_i k_v^{(i)}$ from the eight main vibrational modes. The experimentally obtained temporal profiles of the laser-induced electron detachment reflect the energy distributions at the time of laser excitation. To obtain the cooling rates, these energy distributions were simulated with the rate constants for electron detachment and IR-photon emission.

B. Simulation of time-dependent energy distributions

The energy distribution imparted to the molecules at the time of their production in the ion source is not known. Although we cannot expect that the distribution reaches rigorous equilibrium, it is convenient to parametrize the distribution as a canonical equilibrium distribution at some temperature. This procedure generates both the nonzero lower and the upper energy limits to the excitation energy of the extracted molecules. The parameter $T_{\text{eff}}^{\text{ini}}$ determining the distribution is varied to generate an acceptable initial energy distribution. After acceleration of the ions, no further intermolecular energy exchange takes place, and from that point, the distribution of the internal energy is the only relevant quantity in the simulations.

The temporal propagation of the anion internal energy distribution $g(E, t)$ was calculated as

$$\begin{aligned} \frac{dg(E, t)}{dt} = & - \left[k_d(E) + \sum_i k_v^{(i)}(E) \right] g(E, t) \\ & + \sum_i k_v^{(i)}(E) g(E + h\nu_i, t). \end{aligned} \quad (5)$$

This is a set of equations valid for all energies in the distribution, describing the loss of some anions via electron detachment with rate constant $k_d(E)$ along with radiative cooling of others given by the radiative terms.

Figure 4(a) shows the internal energy distribution for different storage times in the absence of laser excitation. The depletion by electron detachment occurs from the higher-energy side and is clearly seen for the curves representing the distributions at 0.1 and 1 ms; at 20, 40, 60, and 80 ms, radiative cooling is dominant, and the total intensity is therefore almost unchanged at these times. It is immediately obvious from the simulated curves that radiative cooling has a strong influence on the behavior of the decay rates.

Figure 4(b) shows, as an example, the time evolution of the internal energy distributions after one-photon excitation at 20 ms storage time, where the internal energy distribution at a number of revolutions after photoexcitation is presented. The solid red curve in Fig. 4(b) is the red one in Fig. 4(a), shifted by the photon energy of 1.39 eV. The black colored areas represent detachment in the straight section at the indicated number of turns after laser excitation, i.e., as given by Eq. (1). Although radiative cooling is included in the calculation, the shift of the population to lower energy is too small to be seen on these time scales.

The main effect of the radiative cooling is its influence on the shape of the shifted energy distributions for different laser-firing times. The energy distributions before and after photoexcitation, at 60 and 80 ms storage, are shown in Fig. 4(c), together with the initial distribution. They are used to compare the experimentally obtained temporal profiles of laser-induced detachment with those of spontaneous detachment in Sec. V.

C. Simulation of tracking individual ions

The code for the simulation calculates whether anions at a given initial internal energy are eventually neutralized or not. The branching between electron detachment and vibrational radiation was determined to be proportional to $k_d(E)$ and $k_v^{(i)}(E)$, respectively, by generating random numbers. This process was repeated at every energy, until detachment occurs or E reaches the detachment threshold. For each initial internal energy, 10^5 trajectories were calculated. The survival probabilities of anions were surveyed for initial internal energies E_{ini} above the detachment threshold in steps of 10 cm^{-1} .

V. RESULTS AND DISCUSSION

A typical temporal profile of the neutral yield with a photoenhanced signal by 890-nm laser excitation at 40 ms storage time is shown in Fig. 5. The decreasing component up to 40 ms is spontaneous detachment (autodetachment) of the hot ions produced in the ion source. The photoenhanced signals can also be assigned to delayed electron detachment.

Figure 6 shows the spontaneous detachment component measured with high statistical accuracy. The observed decay in the neutral yield reflects both spontaneous detachment of pentacene anions and collisional neutralization with residual background gases. As discussed above, ion intensities

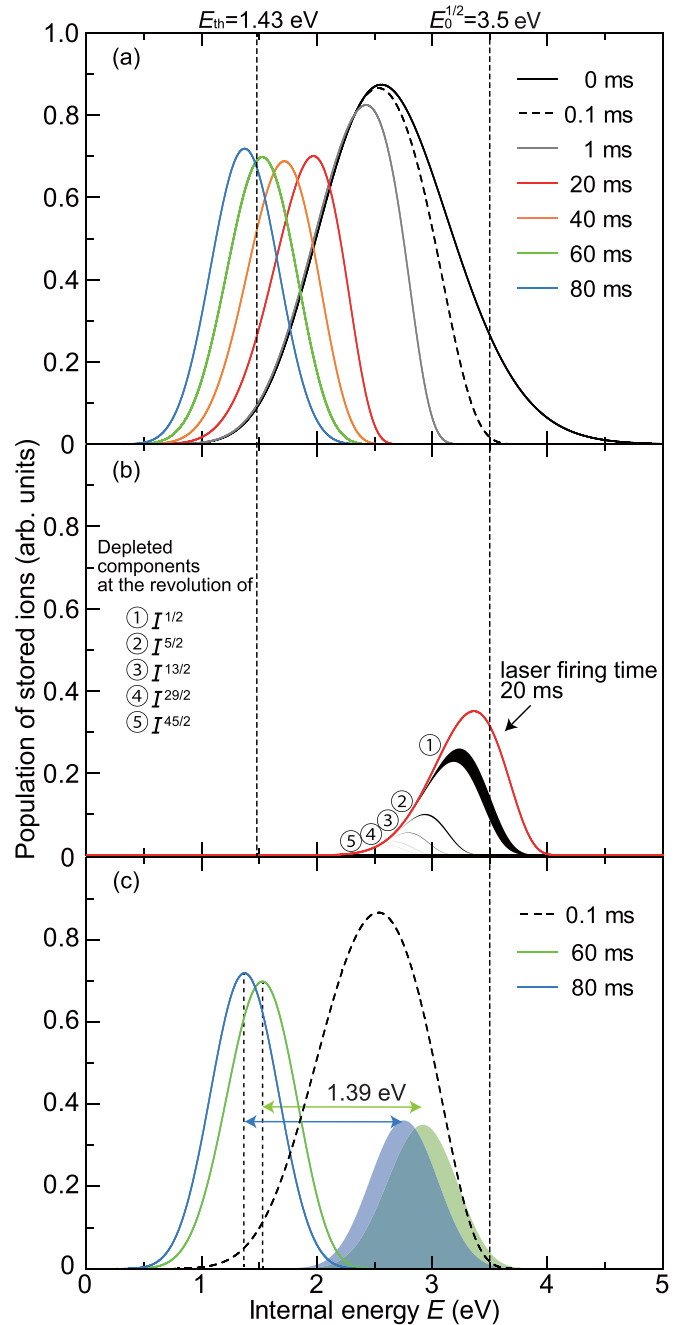


FIG. 4. (a) The internal energy E distribution for storage times of 0, 0.1, 1, 20, 40, 60, and 80 ms (from right to left) without laser excitation. (b) The short time evolution of the energy distributions, which is primarily governed by depletion via electron detachment after one-photon excitation at 20 ms storage time. The red curve is made by shifting the red curve in (a) by the photon energy (1.39 eV); for visibility, the vertical axis is scaled to reflect photoexcitation of half of the stored ions. Black colored areas show the depleted components at the revolution of ① turn 0.5, ② turn 2.5, ③ turn 6.5, ④ turn 14.5, and ⑤ turn 22.5, to be compared with the red circles in Fig. 7. (c) The internal energy distributions for storage times of 60 and 80 ms [the same as in (a)], and those of the photoexcited component shifted by the photon energy (1.39 eV); for visibility, the vertical axis is again scaled. They are compared with the E distribution at 0.1 ms [the same as in (a)].

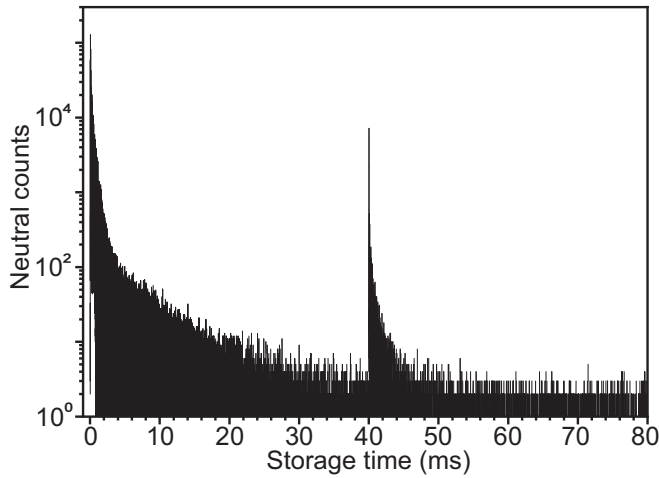


FIG. 5. A typical example of the raw detected neutral yield as a function of storage time. Here, an 890-nm laser pulse was introduced at 40 ms.

extracted after storage times from 10 to 80 ms (the beam dump) are used to study this collision-induced component, which is proportional to the number of stored ions. We confirmed that depletion of the beam is represented by a single-exponential function. Thus, with regard to the neutral yield, a simple exponential reduction, with the same decay constant obtained above and normalized at the 60–80-ms interval (where collisional detachment dominates), yields a straightforward determination of the neutral yield from collisional detachment. By subtracting this function (along with contributions from MCP dark counts) from the observed neutral decay curve, we finally arrive at the intrinsic spontaneous detachment behavior of the pentacene anions. As seen from Fig. 6, it shows the characteristic decrease of a quasiexponen-

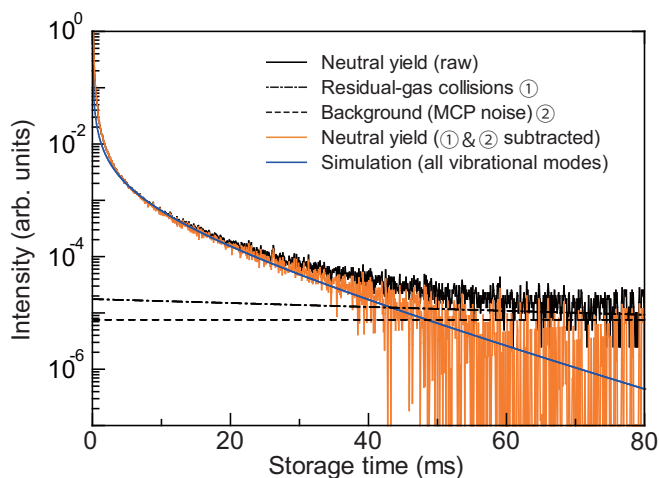


FIG. 6. The temporal profile of the neutral yields originating from spontaneous detachment. The raw temporal profile (upper solid black line) and the profile (lower solid orange line) after subtracting the component due to the residual-gas collisions (dash-dotted black line) are shown along with the background level of MCP noises (dashed black line). The simulated profile is shown as a solid blue curve.

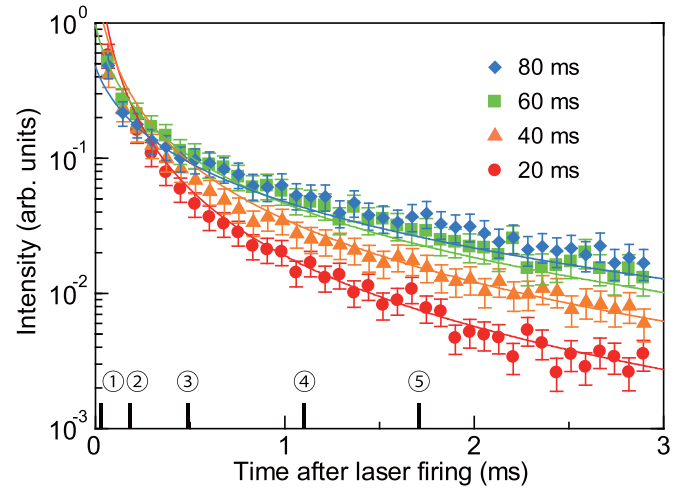


FIG. 7. The temporal profiles of the laser-induced neutral yields for ions stored for 20 ms (red circles), 40 ms (orange triangles), 60 ms (green squares), and 80 ms (blue diamonds) before laser firing. The spectra are normalized to the number of stored ions at the time the laser is fired and to the laser intensity. The contributions from spontaneous detachment and residual-gas collisions have been subtracted. The error bars are calculated by adding statistical and systematic errors in quadrature. The latter is larger and dominated by fluctuations of the stored ion intensities for normalization from betatron oscillations. The solid curves represent simulated decay profiles. The solid black ticks numbered from ① to ⑤ refer to the time regions for which the energy distributions of the ions stored for 20 ms are shown on Fig. 4(b). See the details in the text.

tial function at long times (> 30 ms). This will be discussed in Sec. VB in detail.

Temporal profiles of the neutral yields after laser firing at several different storage times are shown in Fig. 7 for short postexcitation times. The five numbered ticks show the specific storage time region given by the black colored areas in Fig. 4(b) after laser irradiation. Clearly, the temporal behavior in this time range changes with storage time before excitation, with a slower decrease for longer storage times. This tendency reflects the fact that the slope or tail of the high-energy side of the energy distribution in the energy window for these times is shaped by radiative cooling. From this dependence we obtain the optimized correction factor S_v , and thus the cooling rates, as described in the next section. The simulated temporal profiles of the neutral yields obtained with the optimized S_v are shown by the solid curves.

A. Estimation of cooling rates

In this section we first analyze the laser-induced profiles and show how our simulation explains the observed behavior well with optimized parameters. Next, we revisit the temporal profile of the spontaneous detachment and reproduce the observed behavior with the same simulations that are applied to the laser-induced temporal profiles.

First, the simulated temporal profiles were optimized using the two fitting parameters $T_{\text{eff}}^{\text{ini}}$ and S_v , common for all of the experimental data. The calculated χ^2 values are shown in Fig. 8. The best fit was determined to be $(T_{\text{eff}}^{\text{ini}}, S_v) =$

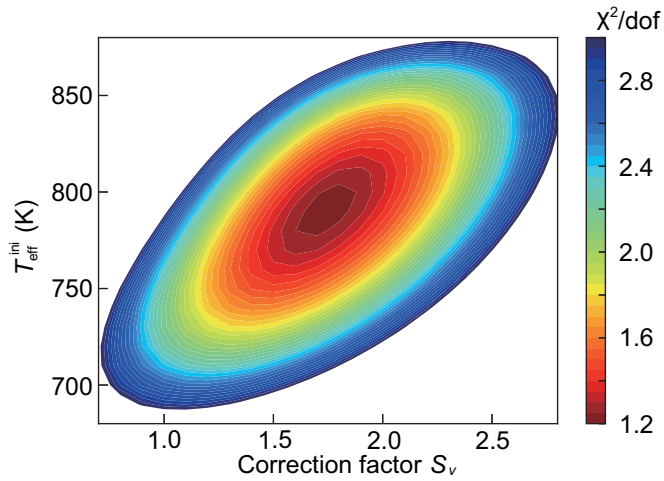


FIG. 8. A contour plot of χ^2/dof as a function of the initial effective temperature $T_{\text{eff}}^{\text{ini}}$ and the correction factor S_v for the A coefficients of IR emission.

(790_{-60}^{+50} K, $1.7_{-0.5}^{+0.7}$) with $\chi^2/\text{dof} = 1.22$, where dof is the number of degrees of freedom. The relatively low fitted initial effective temperature of 790 K reflects the condition of the laser desorption source; production of intact molecules requires a low laser pulse energy to avoid excessive amounts of fragmented ions. We note that the upper edge of the energy distributions produced in the source is close to the cutoff energy for anions that can survive the time of transfer into the ring. As such, a thermal distribution is a weaker assumption about the initial energy distribution than it may appear at first sight. The correction factor of 1.7 is also reasonable, considering that the analogous factors for the carbon cluster anions (C_n^- , $n = 4-7$) obtained previously with the same procedure are also on the order of unity [10]. Note that a single correction factor is used for all vibrational transitions for simplicity. As already shown in Fig. 7, the temporal evolution is well reproduced by our simulation. The possible disagreement at 80 ms suggests a slightly slower cooling at the long times than simulated. The fitting may be improved by relaxing the constraint that the overall analysis shares the same single value of S_v .

Next, we compared the spontaneous temporal profile with the simulation results with the same optimized parameters. Again as already shown in Fig. 6, the agreement of the simulation taking account of all vibrational modes is excellent.

To discuss this in more detail, we focus on the short time range to compare with the laser-induced temporal profile shown in Fig. 9. We found that the spontaneous temporal profile is similar to the laser-induced profile of the neutral yields observed for 60 or 80 ms storage before laser firing. This implies that the internal energy at these times are identical, leading to the statement that absorption of a 890-nm ($= 1.39$ eV) photon is equivalent to the radiative cooling power during 60 or 80 ms ~ 20 eV/s on average, which is consistent with the peak shift in Fig. 4(c). This cooling rate is much lower than those for PAH cations cooled electronically (typically 100 eV/s), while it is naturally

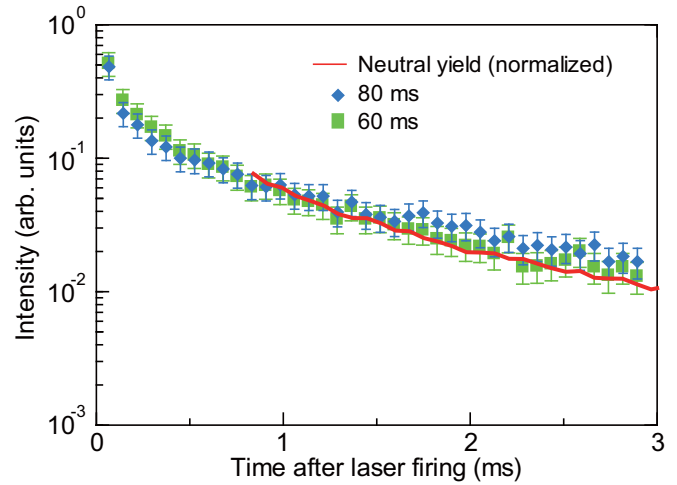


FIG. 9. The temporal profile of the neutral yields originating from spontaneous detachment and those for laser-induced profiles at 60 and 80 ms storage times, zoomed in the time region up to 3 ms. Note that for the spontaneous decays shown by the red curve, the region prior to the time of the kicking out of the unwanted ions at $707.8 \mu\text{s}$ is not shown.

higher than the vibrational cooling rates for smaller PAH cations because of higher dipole moment derivatives and the larger number of IR active vibrational modes [14].

B. Anion survival probabilities

Figure 10 shows the survival probabilities $f(E_{\text{ini}})$ as a function of the initial internal energy E_{ini} obtained by the Monte Carlo simulation. Most of the anions do not emit electrons below $E_{\text{ini}} \approx 1.8$ eV (an excess energy of around 0.4 eV), whereas the survival probability rapidly decreases above that energy. The shift of 0.4 eV up from the electron affinity is due

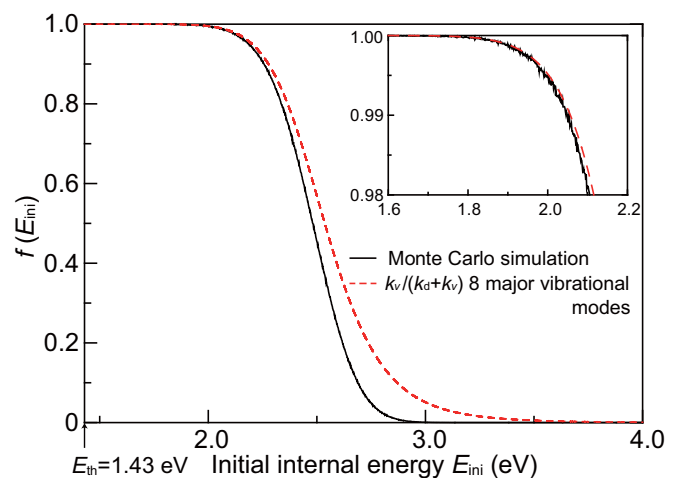
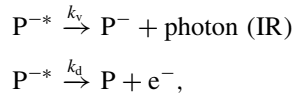


FIG. 10. Survival probabilities $f(E_{\text{ini}})$ as a function of the initial internal energy E_{ini} . The solid black curve shows a Monte Carlo simulation. The dashed red curve is $f(E_{\text{ini}}) = k_v / (k_d + k_v)$, where the eight major vibration modes are taken into account. The inset shows a zoomed view for the region where the difference in the two curves starts to become visible.

to a combination of the large heat capacity and the presence of the radiative cooling.

If emission of a single IR photon provides significant stabilization of the anion, the effect is nearly the same for all such modes. In other words, stabilization is governed by the radiative cooling rate constants rather than the emitted powers. This requires that the emitted photon energy is sufficiently high. Then, $f(E_{\text{ini}})$ should be possible to express as the simple competitive rate equation as an approximation of the single-photon quenching scheme as follows:



where P^{-*} , P^- , and P are pentacene anions above the detachment threshold, those stabilized by radiation, and neutral pentacene, respectively. k_v is the sum of the vibrational cooling rate constants over the vibrational modes responsible for single-photon quenching. The numbers of the P^{-*} , P^- , and P , denoted as $N_{P^{-*}}(t)$, $N_{P^-}(t)$, and $N_P(t)$, respectively, are given by

$$\begin{aligned} N_{P^{-*}}(t) &= e^{-(k_d+k_v)t}, \\ N_{P^-}(t) &= \frac{k_v}{k_d+k_v} [1 - e^{-(k_d+k_v)t}], \\ N_P(t) &= \frac{k_d}{k_d+k_v} [1 - e^{-(k_d+k_v)t}], \end{aligned} \quad (6)$$

assuming the initial conditions of $N_{P^{-*}}(0) = 1$ and $N_{P^-}(0) = N_P(0) = 0$. These lead to the following equation for the time-dependent survival probability:

$$\begin{aligned} f(E_{\text{ini}}, t) &= N_{P^{-*}}(t) + N_{P^-}(t) \\ &= \frac{k_v}{k_d+k_v} + \frac{k_d}{k_d+k_v} e^{-(k_d+k_v)t}, \end{aligned} \quad (7)$$

where k_d and k_v both depend on the initial internal energy E_{ini} . By taking $t \rightarrow \infty$, we obtain

$$f(E_{\text{ini}}) = k_v / (k_d + k_v) \quad (8)$$

as the ultimate survival probability of the ions.

In the low-energy region or at long storage times, the eight major vibrational modes (the main contributors to vibrational radiative cooling shown in Fig. 3) may efficiently quench electron detachment by single-photon emission because the photon energies are relatively large, the lowest being 846 cm^{-1} ($= 0.105 \text{ eV}$). From the temporal evolution of the internal energy distribution in Fig. 4(a), when we focus on the time of 80 ms without laser irradiation, the component leading to electron detachment is located in the region above the E_{th} (1.43 eV) up to around 2 eV. At 2 eV, the electron detachment rate is $k_d = 0.31 \text{ s}^{-1}$ [Fig. 3(a)], and emission of a single photon with energy larger than 846 cm^{-1} lowers k_d below 0.06 s^{-1} . These are all sufficient for quenching, and we can use the approximation that single-photon emission from any of the eight major vibrational modes quenches electron detachment. The sum of the radiative cooling rates by the eight major modes ($k_v^{8\text{-modes}}$) can be regarded as k_v at energies below 2 eV. As shown in Fig. 3(b), $k_v^{8\text{-modes}}$ is 64.6 s^{-1} at 2 eV and varies slowly with E . The dashed red curve in Fig. 10 shows $f(E_{\text{ini}})$

calculated by Eq. (8). At low initial internal energies E_{ini} above E_{th} they agree well, and they begin to deviate as E_{ini} increases. This is very reasonable because single-IR-photon quenching indeed takes place for lower E_{ini} , while the single-photon quenching is a less accurate description for higher E_{ini} .

In the longer time region of spontaneous detachment, we noticed a quasiexponentially decreasing character of the neutral yield. We therefore extended the simulation time to 1 s (Fig. 6) and confirmed that a (numerically) exact exponential with a decay constant of 67.5 s^{-1} is observed around 100 ms. The quasiexponential behavior supports the single-photon quenching scheme, where the decay is governed exclusively by k_v rather than k_d . The decay constant agrees reasonably well with k_v near the 2-eV region.

VI. CONCLUSION

To understand the deexcitation dynamics of pentacene anions isolated in vacuum, we stored them in the TMU E-ring and observed the neutral yields originating from electron detachment for every revolution in the time range of about 80 ms. We observed spontaneous detachment in the time range up to 40 ms. The photoinduced delayed detachment was also measured by introducing a light pulse from a tunable OPO laser at 890 nm wavelength under merging conditions. We found that the temporal profile of photoinduced delayed detachment shows a slower decrease for longer storage times, when we changed the storage time from 20 ms up to 80 ms before photoexcitation. This behavior reflects the temporal evolution of the internal energy distribution determined by electron detachment and radiative cooling. With the aid of a simulation based on a statistical description of these processes, we quantitatively reproduced the vibrational cooling that takes place in a few-tens-of-milliseconds time range.

Using the experimentally scaled vibrational cooling rate, we discussed the quasiexponential decrease in the long time region of the temporal profile of the spontaneous detachment. We concluded that the observed quasiexponential decrease originates in single-photon quenching of electron detachment in the internal energy region close to the detachment threshold E_{th} .

Finally, it should be pointed out that the single-IR-photon quenching is not peculiar, but should be commonly observable. It is essentially determined by the photon energy relative to the slope of the survival function against electron detachment at the critical internal energy at any given time. In other words, the criterion for whether the single-photon quenching scheme can be adopted or not is given by the photon energy relative to the heat capacity, i.e., how the loss of one photon affects the reduction of k_d : a smaller heat capacity leads to a larger change in k_d . Thereby, this condition is more easily satisfied for smaller systems. From such a point of view, it is worthwhile to revisit the case of C_5^- and C_7^- , where spontaneous detachment is observed, more carefully. Indeed, we previously observed the exponential-like temporal profile of spontaneous detachment for C_7^- [6], and the temporal profile in a longer time range was recently reported [38].

ACKNOWLEDGMENTS

The authors thank Dr. P. M. Mishra for support of the experiments and calculation of molecular properties and acknowledge Dr. K. Chartkunchand and Dr. N. Kimura for valuable suggestions. This work was supported by JSPS KAKENHI [Grant-in-Aid for Scientific Research (A)

TABLE I. Infrared frequencies and symmetries of vibrational modes for the neutral pentacene molecule. A frequency scaling factor of 0.967 was used for the vibrational wave numbers. This is for the 6-311+G(3df,2p) basis [39].

Mode No.	Symmetry	Frequency (cm ⁻¹)	Mode No.	Symmetry	Frequency (cm ⁻¹)
1	B _{1u}	36.8	26	A _g	627.3
2	A _u	69.2	27	A _u	694.2
3	B _{3g}	98.2	28	B _{1g}	702.6
4	B _{3u}	115.2	29	B _{2u}	718.9
5	B _{2g}	143.3	30	B _{1u}	721.9
6	B _{1u}	186.0	31	B _{3g}	727.2
7	B _{1g}	230.5	32	B _{2g}	731.3
8	A _u	231.2	33	A _g	736.5
9	A _g	254.6	34	A _u	749.9
10	B _{3g}	283.8	35	B _{2g}	756.7
11	B _{2g}	336.0	36	A _g	767.6
12	B _{3u}	350.5	37	B _{3u}	813.0
13	B _{1u}	370.3	38	B _{2g}	815.3
14	B _{1g}	440.2	39	A _u	821.6
15	B _{1u}	456.6	40	B _{1u}	823.4
16	B _{3g}	457.8	41	B _{2g}	851.0
17	B _{1u}	464.0	42	B _{2u}	858.3
18	B _{3g}	465.3	43	B _{3g}	872.1
19	B _{2u}	474.4	44	A _u	881.0
20	B _{1g}	497.0	45	B _{3u}	895.8
21	A _u	508.1	46	B _{2g}	898.8
22	B _{2g}	535.9	47	B _{1u}	905.6
23	B _{3u}	561.2	48	B _{1g}	910.3
24	A _g	596.7	49	B _{3g}	950.6
25	B _{2u}	619.4	50	B _{1u}	951.2

21H04447 and Grant-in-Aid for Early-Career Scientists 20K14386] and the RIKEN Pioneering Projects.

APPENDIX: CALCULATED VIBRATIONAL PROPERTIES OF NEUTRAL AND ANIONIC PENTACENE MOLECULES

In this Appendix, the calculated vibrational properties of the 102 vibrational modes of the neutral molecule (Table I) and the anion (Table II) are given.

TABLE I. (Continued.)

Mode No.	Symmetry	Frequency (cm ⁻¹)	Mode No.	Symmetry	Frequency (cm ⁻¹)
51	B _{2g}	965.2	77	B _{3u}	1429.2
52	A _u	965.2	78	B _{2u}	1433.0
53	B _{2u}	979.9	79	A _g	1447.4
54	A _g	982.8	80	B _{2u}	1489.6
55	B _{2u}	1092.1	81	A _g	1504.3
56	B _{3u}	1106.8	82	A _g	1520.5
57	B _{1g}	1121.6	83	B _{2u}	1522.9
58	A _g	1148.2	84	B _{1g}	1537.7
59	B _{2u}	1151.6	85	B _{1g}	1574.7
60	B _{1g}	1163.0	86	B _{3u}	1583.2
61	A _g	1167.3	87	B _{1g}	1612.5
62	B _{3u}	1172.5	88	B _{3u}	1613.2
63	B _{1g}	1199.7	89	B _{3u}	3057.1
64	B _{2u}	1207.9	90	B _{1g}	3058.4
65	B _{3u}	1257.1	91	A _g	3058.8
66	B _{1g}	1257.3	92	B _{3u}	3060.4
67	B _{1g}	1274.1	93	B _{2u}	3060.5
68	B _{3u}	1279.5	94	B _{1g}	3061.4
69	A _g	1284.5	95	B _{3u}	3063.0
70	B _{2u}	1316.1	96	A _g	3063.8
71	B _{3u}	1334.2	97	B _{2u}	3065.9
72	A _g	1358.9	98	A _g	3066.8
73	B _{2u}	1363.5	99	B _{1g}	3077.8
74	B _{2u}	1377.5	100	B _{3u}	3077.8
75	B _{1g}	1378.5	101	B _{2u}	3089.0
76	A _g	1382.3	102	A _g	3089.1

TABLE II. Infrared frequencies, symmetries, intensities, and Einstein A coefficients for the anionic pentacene molecule. A frequency scaling factor of 0.967 was used for the vibrational wave numbers. This is for the 6-311+G(3df,2p) basis [39].

Mode No.	Symmetry	Frequency (cm ⁻¹)	Intensity (km/mol)	A coefficient (s ⁻¹)	Mode No.	Symmetry	Frequency (cm ⁻¹)	Intensity (km/mol)	A coefficient (s ⁻¹)
1	B _{1u}	37.2	0.28	0	52	B _{2g}	920.4	0	0
2	A _u	66.8	0	0	53	B _{2u}	994.4	38.09	4.717
3	B _{3g}	99.2	0	0	54	A _g	995.7	0	0
4	B _{3u}	114.5	1.37	0.002	55	B _{3u}	1089.7	11.16	1.660
5	B _{2g}	142.5	0	0	56	B _{1g}	1102.9	0	0
6	B _{1u}	185.4	0.91	0.004	57	B _{2u}	1123.3	0.01	0.001
7	B _{1g}	228.0	0	0	58	A _g	1133.4	0	0
8	A _u	229.4	0	0	59	B _{1g}	1138.4	0	0
9	A _g	253.7	0	0	60	B _{2u}	1145.4	173.11	28.445
10	B _{3g}	299.4	0	0	61	B _{3u}	1156.2	0.68	0.114
11	B _{2g}	312.7	0	0	62	A _g	1168.5	0	0
12	B _{1u}	344.2	0.10	0.002	63	B _{1g}	1199.6	0	0
13	B _{3u}	348.3	0.53	0.008	64	B _{2u}	1202.6	173.85	31.49
14	B _{1g}	440.5	0	0	65	B _{3u}	1246.1	0.50	0.098
15	B _{1u}	449.4	21.36	0.540	66	B _{1g}	1248.0	0	0
16	B _{3g}	453.9	0	0	67	B _{1g}	1255.1	0	0
17	B _{3g}	456.1	0	0	68	A _g	1260.2	0	0
18	B _{1u}	456.4	13.26	0.346	69	B _{3u}	1266.8	17.26	3.469
19	B _{2u}	471.0	55.63	1.545	70	B _{3u}	1308.3	2.05	0.440
20	B _{1g}	497.6	0	0	71	B _{2u}	1328.6	1420.77	314.106
21	A _u	536.8	0	0	72	A _g	1339.8	0	0
22	B _{2g}	547.2	0	0	73	B _{2u}	1347.1	98.20	22.319
23	B _{3u}	566.5	0.65	0.026	74	B _{2u}	1355.6	357.51	82.279
24	A _g	596.1	0	0	75	A _g	1358.4	0	0
25	B _{2u}	616.8	16.76	0.799	76	B _{1g}	1372.7	0	0
26	A _g	618.7	0	0	77	B _{3u}	1416.2	0.34	0.084
27	A _u	692.2	0	0	78	B _{2u}	1423.0	5.08	1.288
28	B _{1u}	695.7	99.13	6.008	79	A _g	1447.2	0	0
29	B _{3g}	701.4	0	0	80	B _{2u}	1470.3	131.20	35.522
30	B _{1g}	702.0	0	0	81	B _{1g}	1473.5	0	0
31	B _{2g}	713.9	0	0	82	A _g	1481.3	0	0
32	B _{2u}	722.9	27.37	1.791	83	B _{1g}	1498.1	0	0
33	A _g	727.4	0	0	84	B _{2u}	1503.4	321.07	90.883
34	A _u	735.5	0	0	85	A _g	1507.8	0	0
35	B _{2g}	749.1	0	0	86	B _{3u}	1542.3	2.62	0.781
36	B _{2g}	765.3	0	0	87	B _{3u}	1555.7	0.12	0.037
37	B _{1u}	766.7	16.29	1.199	88	B _{1g}	1572.6	0	0
38	A _g	767.2	0	0	89	B _{3u}	3029.3	2.90	3.337
39	A _u	788.5	0	0	90	A _g	3030.6	0	0
40	B _{2g}	808.3	0	0	91	B _{1g}	3031.1	0	0
41	B _{3u}	808.7	0.29	0.024	92	B _{3u}	3033.0	0.38	0.442
42	B _{3g}	819.6	0	0	93	B _{2u}	3033.4	0.46	0.536
43	A _u	837.1	0	0	94	B _{1g}	3034.5	0	0
44	B _{1u}	845.9	105.57	9.461	95	B _{3u}	3037.0	146.21	168.903
45	B _{2g}	851.0	0	0	96	A _g	3037.5	0	0
46	B _{2u}	856.9	2.69	0.248	97	B _{2u}	3040.1	0	0
47	B _{3u}	889.0	0.64	0.063	98	A _g	3041.7	0	0
48	B _{3g}	901.7	0	0	99	B _{1g}	3052.8	0	0
49	B _{1u}	902.1	16.50	1.682	100	B _{3u}	3052.9	152.51	178.029
50	B _{1g}	904.7	0	0	101	B _{2u}	3067.8	212.41	250.376
51	A _u	920.4	0	0	102	A _g	3068.1	0	0

- [1] P. Ferrari, E. Janssens, P. Lievens, and K. Hansen, *Int. Rev. Phys. Chem.* **38**, 405 (2019).
- [2] H. T. Schmidt, *Phys. Scr.* **2015**, 014063 (2015).
- [3] R. Wester, *J. Phys. B* **42**, 154001 (2009).
- [4] L. H. Andersen, O. Heber, and D. Zajfman, *J. Phys. B* **37**, R57 (2004).
- [5] M. Goto, A. Sundén, H. Shiromaru, J. Matsumoto, H. Tanuma, T. Azuma, and K. Hansen, *J. Chem. Phys.* **139**, 054306 (2013).
- [6] K. Najafian, M. S. Pettersson, B. Dynefors, H. Shiromaru, J. Matsumoto, H. Tanuma, T. Furukawa, T. Azuma, and K. Hansen, *J. Chem. Phys.* **140**, 104311 (2014).
- [7] G. Ito, T. Furukawa, H. Tanuma, J. Matsumoto, H. Shiromaru, T. Majima, M. Goto, T. Azuma, and K. Hansen, *Phys. Rev. Lett.* **112**, 183001 (2014).
- [8] V. Chandrasekaran, B. Kafle, A. Prabhakaran, O. Heber, M. Rappaport, H. Rubinstein, D. Schwalm, Y. Toker, and D. Zajfman, *J. Phys. Chem. Lett.* **5**, 4078 (2014).
- [9] N. Kono, T. Furukawa, H. Tanuma, J. Matsumoto, H. Shiromaru, T. Azuma, K. Najafian, M. S. Pettersson, B. Dynefors, and K. Hansen, *Phys. Chem. Chem. Phys.* **17**, 24732 (2015).
- [10] N. Kono, R. Suzuki, T. Furukawa, J. Matsumoto, H. Tanuma, H. Shiromaru, T. Azuma, and K. Hansen, *Phys. Rev. A* **98**, 063434 (2018).
- [11] A. G. G. M. Tielens, *Rev. Mod. Phys.* **85**, 1021 (2013).
- [12] A. G. G. M. Tielens, *Annu. Rev. Astron. Astrophys.* **46**, 289 (2008).
- [13] S. Martin, J. Bernard, R. Brédy, B. Concina, C. Joblin, M. Ji, C. Ortega, and L. Chen, *Phys. Rev. Lett.* **110**, 063003 (2013).
- [14] S. Martin, M. Ji, J. Bernard, R. Brédy, B. Concina, A. R. Allouche, C. Joblin, C. Ortega, G. Montagne, A. Cassimi, Y. Ngono-Ravache, and L. Chen, *Phys. Rev. A* **92**, 053425 (2015).
- [15] S. Martin, J. Matsumoto, N. Kono, M.-C. Ji, R. Brédy, J. Bernard, A. Cassimi, and L. Chen, *Nucl. Instrum. Methods Phys. Res. Sect. B* **408**, 209 (2017).
- [16] S. Martin, L. Chen, A. Al-Mogeeth, and J. Bernard, *Phys. Rev. A* **99**, 012712 (2019).
- [17] M. H. Stockett, J. N. Bull, J. T. Buntine, E. Carrascosa, M. Ji, N. Kono, H. T. Schmidt, and H. Zettergren, *J. Chem. Phys.* **153**, 154303 (2020).
- [18] M. Saito, H. Kubota, K. Yamasa, K. Suzuki, T. Majima, and H. Tsuchida, *Phys. Rev. A* **102**, 012820 (2020).
- [19] K. Hansen and E. E. B. Campbell, *J. Chem. Phys.* **104**, 5012 (1996).
- [20] J. U. Andersen, C. Brink, P. Hvelplund, M. O. Larsson, B. Bech Nielsen, and H. Shen, *Phys. Rev. Lett.* **77**, 3991 (1996).
- [21] R. V. Kathymov, M. V. Muftakhov, and P. V. Shchukin, *Rapid Commun. Mass Spectrom.* **31**, 1729 (2017).
- [22] T. J. Millar, C. Walsh, and T. A. Field, *Chem. Rev.* **117**, 1765 (2017).
- [23] V. Wakelam and E. Herbst, *Astrophys. J.* **680**, 371 (2008).
- [24] T. Shida and S. Iwata, *J. Am. Chem. Soc.* **95**, 3473 (1973).
- [25] T. Masubuchi, Y. Sugawara, and A. Nakajima, *J. Chem. Phys.* **145**, 244306 (2016).
- [26] T. M. Halasinski, D. M. Hudgins, F. Salama, L. J. Allamandola, and T. Bally, *J. Phys. Chem. A* **104**, 7484 (2000).
- [27] J. Aihara, K. Fujiwara, A. Harada, H. Ichikawa, K. Fukushima, F. Hirota, and T. Ishida, *J. Mol. Struct.: THEOCHEM* **366**, 219 (1996).
- [28] S. Hirata, M. Head-Gordon, J. Szczepanski, and M. Vala, *J. Phys. Chem. A* **107**, 4940 (2003).
- [29] C. Lee, W. Yang, and R. G. Parr, *Phys. Rev. B* **37**, 785 (1988).
- [30] A. D. Becke, *J. Chem. Phys.* **98**, 5648 (1993).
- [31] M. J. Frisch, G. W. Trucks, H. B. Schlegel, G. E. Scuseria, M. A. Robb, J. R. Cheeseman, G. Scalmani, V. Barone, B. Mennucci, G. A. Petersson, H. Nakatsuji, M. Caricato, X. Li, H. P. Hratchian, A. F. Izmaylov, J. Bloino, G. Zheng, J. L. Sonnenberg, M. Hada, M. Ehara *et al.*, Gaussian 09 Revision A.1, Gaussian Inc., Wallingford, CT, 2009.
- [32] S. R. Langhoff, *J. Phys. Chem.* **100**, 2819 (1996).
- [33] D. Hudgins and L. J. Allamandola, *J. Phys. Chem.* **99**, 8978 (1995).
- [34] J. Szczepanski, C. Wehlburg, and M. Vala, *Chem. Phys. Lett.* **232**, 221 (1995).
- [35] S. Jinno, T. Takao, K. Hanada, M. Goto, K. Okuno, H. Tanuma, T. Azuma, and H. Shiromaru, *Nucl. Instrum. Methods Phys. Res. Sect. A* **572**, 568 (2007).
- [36] T. Furukawa, G. Ito, M. Goto, T. Majima, H. Tanuma, J. Matsumoto, H. Shiromaru, K. Hansen, and T. Azuma, *Nucl. Instrum. Methods Phys. Res. Sect. B* **354**, 192 (2015).
- [37] J. U. Andersen, E. Bonderup, and K. Hansen, *J. Phys. B: At., Mol. Opt. Phys.* **35**, R1 (2002).
- [38] M. H. Stockett, J. N. Bull, J. T. Buntine, E. Carrascosa, E. K. Andersson, M. Gatchell, M. Kaminska, R. F. Nascimento, H. Cederquist, H. T. Schmidt, and H. Zettergren, *Eur. Phys. J. D* **74**, 150 (2020).
- [39] R. D. Johnson III, NIST Computational Chemistry Comparison and Benchmark Database, NIST Standard Reference Database No. 101, Release 21, August 2020, <http://cccbdb.nist.gov/>.